Utilization of carbide slag in autoclaved aerated concrete preparation

Kai Luo (ksiluo@swust.edu.cn)
Southwest University of Science and Technology
Ke Peng
Southwest University of Science and Technology
Jun Li
Southwest University of Science and Technology
Zhongyuan Lu
Southwest University of Science and Technology
Jun Jiang
Southwest University of Science and Technology

Research Article

Keywords: autoclaved aerated concrete, carbide slag, performances, pore structure

Posted Date: May 26th, 2022

DOI: https://doi.org/10.21203/rs.3.rs-1557137/v1

Abstract

Lime is one of the main raw materials necessary for the production of autoclaved aerated concrete (AAC). The preparation of lime through calcining limestone directly/indirectly emits large amount of CO_2 due to the limestone decomposition and energy consumption. In this study, AAC was proposed by using modified carbide slag (MCS) instead of lime, which can effectively utilize solid wastes and reduce the CO_2 emission. Results showed in the first two hours of hydration, the heat release rate of MCS was higher than that of lime, and the cumulative hydration heat of lime and MCS within 30 h is 206.1 J/g and 204.3 J/g, respectively. MCS can not only improve the fluidity of slurry, but also enhance the gas-foaming rate. Cumulative pore volume increased with the increase of MCS content in AAC. Tobermorite, quartz, katoite, anhydrite and calcite are the main minerals in AAC. With the increase of MCS content, the density and strength of AAC decrease and the thermal insulation performance increase. When the MCS content is 100%, the AAC density is 594 kg/m^3, the compressive strength is 3.6 MPa and the thermal conductivity is 0.141 $W \cdot m^{-1} \cdot K^{-1}$, meets B06 A3.5 in Chinese standard GB 11968 – 2019.

1. Introduction

Autoclaved aerated concrete is a kind of porous concrete product, which is made of fly ash, lime, cement, gypsum and sand as the main raw materials, adding an appropriate amount of air entraining agent, through the process of batching, mixing, pouring, static stop curing, cutting and high-pressure steam curing (Qu and Zhao 2017; Bhosale et al. 2019). It was widely used in building materials because of its light weight, good heat insulation performance, sound insulation performance, anti-seismic and flame retardant performance, convenient construction and other characteristics (Narayanan and Ramamurthy 2000; Bhosale et al. 2020). However, the main problem of AAC production is the consumption of natural resources and the related CO_2 emissions. The consumption of natural resources mainly includes the consumption of fly ash and sand (Albayrak et al. 2007). The generation process of lime requires energy consumption, and the calcination and decomposition of limestone will also emit a large amount of CO_2. In recent years, more and more industrial solid wastes (such as coal gangue (Wang et al. 2016), iron ore tailings (Ma et al. 2016), graphite tailings (Peng et al. 2021), red gypsum (Cai et al. 2021), etc.) are used to replace fly ash and sand to produce AAC, in order to better alleviate the pressure of solid waste pollution and natural resource depletion. However, there are few researches on solid waste which can be used to replace lime, but CO_2 emission still needs to be paid attention to. In this sense, the research on the utilization of industrial by-products in AAC, especially the research on lime substitutes, is of great significance for waste recycling and environmental protection.

Carbide slag (CS), a strong alkaline solid waste consisting mainly of $Ca(OH)_2$ after hydrolysis of calcium carbide to acetylene (C_2H_2). In China, the stock of CS pile continues to increase, and the production capacity reached about 40 million tons in 2019 (Li and Yi 2020). Its continuous increase aggravates environmental pollution (Yang et al. 2021). The protection of the environment and the recycling of natural resources are the necessary conditions for sustainable development. Therefore, the recycling of CS has attracted a lot of researchers' attention (Gong et al. 2020; Chindaprasirt et al. 2020; Dulaimi et al. 2020;

Phoongernkham et al. 2020). Some researchers use CS as a calcium-containing additive to improve the properties of geopolymers (Amnadnua et al. 2013; Hanjitsuwan et al. 2017). In addition, CS can be used as a soil stabilizer (Horpibulsuk et al. 2012), and studies have shown that CS has similar properties to lime in stabilizing clay (Phummiphan et al. 2017). Moreover, CS is combined with silica rich wastes such as rice husk ash (Nshimiyimana et al. 2019), fly ash (Horpibulsuk et al. 2014) and bagasse (Rattanashotinunt et al. 2013) in concrete, which can be used as a green material to partially replace ordinary Portland cement. Studies have shown that CS can form cementitious materials similar to cement when mixed with a certain amount of pozzolanic materials (Cong and Mei 2021; Ashish and Verma 2019; Ashish 2019). However, the consumption is small compared to the production of CS. Applying it to building materials is a simple and effective way and can be used in large quantities. In fact, CS is mainly consisting of $Ca(OH)_2$, which is the essential component in lime-based materials. That is, lime can be obtained by CS.

In this study, AAC was produced by using modified CS (MCS) instead of lime in different proportions (25%, 50%, 75%, 100%). The comprehensive performance of AAC prepared by MCS and lime was evaluated and compared systematically.

2. Experimental Program

2.1 Materials

Table 1
Chemical composition of materials (wt%)

Elements	CaO	SiO_2	SO_3	Al_2O_3	MgO	Fe_2O_3	TiO_2	SrO	Na_2O	ZrO_2	LOI
Cement	78.99	12.17	3.42	2.83	1.45	0.35	0.11	0.08	0.03	0.02	0.51
CS	66.14	2.58	0.56	1.11	0.11	7.94	0.50	-	0.06	-	24.05
MCS	83.19	3.24	0.71	1.4	0.14	9.99	0.63	-	0.08	-	0.41
Lime	89.95	2.35	-	0.95	2.13	-	-	-	-	-	4.58
Fly ash	9.64	54.98	1.52	18.97	0.77	9.50	2.11	0.31	0.23	0.07	1.89

Portland cement P·O 42.5R, carbide slag (CS), fly ash, gypsum and Al powder were used in this study. CS was modified (MCS) at 550°C in high temperature oven. The chemical composition of cement, fly ash and CS was shown in Table 1, the main mineral compositions of cement are C_3S, C_2S, C_3A, C_4AF as shown in Fig. 1, and it comes from Sichuan Esheng (Leshan) Cement Group. CS, its mineral compositions are $Ca(OH)_2$ as shown in Fig. 1, it comes from Sichuan Jinlu Group. The mineral phases of Lime and modified CS (MCS) are CaO as shown in Fig. 1. The mineral phases of fly ash is CaO as shown in Fig. 1. The particle size distributions of cement, fly ash, lime and MCS are presented in Fig. 2.

2.2 Preparation

Table 2
Mix design of the autoclaved aerated concrete

ID	Cement	MCS	Lime	Fly ash	Gypsum	Al powder	W/B
AAC-1	5%	0	25.00%	67%	3%	0.10%	0.6
AAC-2	5%	6.25%	18.75%	67%	3%	0.10%	0.6
AAC-3	5%	12.50%	12.50%	67%	3%	0.10%	0.6
AAC-4	5%	18.75%	6.25%	67%	3%	0.10%	0.6
AAC-5	5%	25.00%	0	67%	3%	0.10%	0.6

According to the mix design in Table 2, cement, MCS, lime, fly ash and gypsum were weighted and mixed evenly, and then added into the weighed water (60 ℃). After mixing for 60s, Al powder was added and stirred again for 60s. Fresh AAC slurries were injected into steel molds (100 mm × 100 mm ×100 mm). Steel molds containing slurries were cured in a steam curing box (60°C) for 12 h and then demould. Finally, the demoulded sample was put into autoclave for 8 hours (216°C, 2 MPa).

2.3. Test methods

The heat release and heat release rate of lime and MCS were determined by I-Cal 8000 HPC high precision isothermal calorimeter (Calmetrix, America) at 20°C.

Foaming rate test: record the volume of slurry in 500 ml measuring cylinder every 2 min until the slurry stops expanding and the initial slurry volume is 300 ml.

The mechanical properties of the AAC were tested on a mechanical performance testing machine (SANS CMT5105, Shenzhen, China), and the dry density was measured according to GB/T 11968 – 2019.

The thermal conductivity of the AAC with the size of 100 mm×100 mm×100 mm was measured by heat-flow conductometer (DRH-II, Xiangtan Xiangyi Instrument Co.,Ltd., Hunan province, China) according to the Chinese standard GB/T 10294 – 2008.

X-ray diffraction (XRD) was used to determine the mineral composition (using D8 ADVANCE diffractometer (Bruck AXS GmbH, Germany)). The chemical composition of the test raw materials is tested by X-ray fluorescence spectrometry (XRF, Axios, PANalytical, the Netherlands). Observe the microstructure of the sample using a scanning electron microscope (SEM, ULRA 55, Zeiss Instruments, Germany). Thermogravimetric analysis was performed (TG, STA8000, PerkinElmer, USA), in the alumina crucible, the test was carried out at a temperature of 10 ℃/min in a nitrogen stream (50 ml/min) at 25 to 1000 ℃. The pore structure of the matrix was tested with mercury intrusion (automatic hole IV9500, Micromeritics, USA, maximum mercury penetration pressure: 30000 Psi).

3. Results And Discussion

3.1 Hydration heat of lime and MCS pastes

Lime is an indispensable raw material in AAC production, which mainly plays the following roles (Cai et al. 2020; Wu et al. 2020): (a) Provide alkalinity and heat to promote the gas generation of aluminum paste. The reaction rate of aluminum powder is affected by solution temperature and alkalinity. As a traditional foaming agent, aluminum powder reacts with water to produce hydrogen and form bubbles. This process needs to be carried out in alkaline environment, because another product of aluminum powder Aluminium Hydroxide Gel prevents water from contacting with unreacted aluminum powder. The presence of alkali can dissolve aluminum hydroxide to ensure the continuous reaction. (b) Active calcium oxide was provided to promote the formation of C-S-H and tobermorite. AAC is a kind of autoclaved calcium silicate system. The strength of AAC is mainly contributed by C-S-H and tobermorite, and is formed by the hydrothermal reaction of $Ca(OH)_2$ and SiO_2. (c) When lime meets with water, it releases heat and makes the slurry harden rapidly .

The hydration thermal evolution of lime and MCS at 20 ℃ is shown in Fig. 3. The exothermic reaction of lime and MCS is mainly concentrated within 3 h, and the cumulative hydration heat of lime and MCS within 30 h is 206.1 J/g and 204.3 J/g, respectively. Both the lime and MCS exhibit similar hydration thermal evolution behaviors, with only one exothermic peak. The exothermic behavior starts immediately from contact with water and reaches the maximum, as shown in Fig. 3a. In the first two hours of hydration, the heat release rate of MCS was higher than that of lime, and the heat release rate of MCS was 0.0449 w/g for 50.5 min, and that of lime was 0.0447 w/g for 49 min, as shown in Fig. 3b. With the extension of hydration time, the hydration heat release rate of lime exceed MCS after 2 h, as shown in Fig. 3c. The cumulative hydration heat release of MCS is higher than lime within 20 h, and the cumulative hydration heat release of lime gradually exceed MCS after 20 h hydration, as shown in Fig. 3d, Fig. 3e and Fig. 3f, corresponding to the hydration heat release results of Fig. 3a, Fig. 3b and Fig. 3c. The results showed that the CaO activity in MCS was higher than that of lime, and the heat release of MCS was equivalent to that of lime. Therefore, MCS could replace lime as the calcium source of AAC, considering from the perspective of heat release.

3.2. Effects of MCS dosage on properties of slurry

The effects of MCS dosage on slurry fiuidity fluctuated and gas-foaming time are shown in Fig. 4. As shown in Fig. 4, the fluidity of slurry showed an upward trend with the increase of MCS. In contrast, gas-foaming time is decreasing. When MCS was 0%, the foaming time reached a peak of 74min and the fluidity was at the lowest 125mm. Then, with the increase of MCS, the fluidity reached a peak of 160mm and the foaming time gradually decreased to 54min. As shown in Fig. 5, the surface of lime particles is loose and porous, and the shape is irregular. MCS particles are dense and spherical, so the water absorption and fluidity of lime are relatively small, compared with MCS. MCS can not only improve the fluidity of slurry, but also enhance the gas-foaming rate.

The effect of different MCS on the foaming rate of AAC is shown in Fig. 6. With the increase of MCS content, the expansion volume of slurry increased from 214 ml to 220 ml. The addition of MCS can obviously improve the foaming effect and reduce the bulk density of AAC. As shown in Fig. 6, the higher the content of MCS in slurry, the higher the volume expansion rate of slurry. It can be seen from Fig. 6 (b) that

with the increase of MCS content, the time for the slurry to reach the peak value of foaming rate is shortened. When the content of MCS is increased from 0 to 25%, 50%, 75% and 100%, the foaming time is reduced from 24 min to 14 min, and the foaming rate of AAC-1 is the highest, which is 19 ml/min. It can be explained that the content of active Cao in MCS is higher, the formation rate of $Ca(OH)_2$ and the early heating rate and calorific value of the slurry mixed with MCS are higher than those of lime. When the slurry reaches a higher temperature, a large amount of gas will be produced, resulting in foaming and volume expansion of the slurry. As mentioned above, Aluminium Hydroxide Gel can be dissolved in alkaline solution to ensure that the reaction continues. Due to the rapid hydration of MCS, the alkalinity of the slurry can be effectively improved and the initial foaming process of aluminum powder can be ensured.

3.3. Effect of MCS on physical properties of AAC

The effect of MCS on the mechanical properties and dry density of AAC is shown in Fig. 7. The dry density of AAC decreased with the increase of MCS content, and the mechanical properties showed the same trend. With the increase of MCS from 0–100%, the compressive strength decreased from 4.5 MPa to 4.3 MPa, 3.9 MPa, 3.8 MPa and 3.6 MPa, and the dry density decreased from 620 kg/m^3 to 615kg/m^3, 603kg/m^3, 600kg/m^3 and 594kg/m^3. The results obtained meet the AAC of B06 A3.5 in Chinese standard GB 11968 – 2019. Under the same conditions, there is a close relationship between AAC strength and dry density. The decrease of dry density directly leads to the decrease of compressive strength. As mentioned above, compared with lime, the hydration heat release rate of MCS in the early stage is high and the heat release rate is fast, which provides a good environment for the gas generation of aluminum powder, promotes the gas generation effect of aluminum powder, and enhances the volume expansion rate of AAC, so the bulk density of AAC is reduced. When producing AAC with the same bulk density, using MCS as calcareous material can reduce the content of aluminum powder to a certain extent and save the production cost, which is compared with lime.

The effect of MCS on the thermal conductivity and dry density of AAC is shown in Fig. 8. The thermal conductivity of AAC decreased with the increase of MCS content. With the increase of MCS from 0–100%, the thermal conductivity decreased from 0.156 $W{\cdot}m^{-1}{\cdot}K^{-1}$ to 0.152 $W{\cdot}m^{-1}{\cdot}K^{-1}$, 0.145 $W{\cdot}m^{-1}{\cdot}K^{-1}$, 0.143 $W{\cdot}m^{-1}{\cdot}K^{-1}$ and 0.141 $W{\cdot}m^{-1}{\cdot}K^{-1}$. The results obtained meet the AAC of B06 in Chinese standard GB 11968 – 2019. As shown in the figure, the thermal conductivity decreases with the decrease of density. The thermal conductivity of AAC is closely related to the dry density. The smaller the dry density, the greater the matrix porosity, the looser the matrix, and the lower the thermal conductivity.

3.4. Micro properties

3.4.1. Pore structures

MIP results of AAC and hardened aerated concrete (HAC-5) were shown in Fig. 9. Cumulative pore volume increased with the increase of MCS content in AAC, and the cumulative pore volume of the HAC-5 is less than the final AAC-5. The pore size of AAC-1 is mainly distributed around 50 nm, and it increased with the increase of MCS. The pore size of AAC-1 is mainly distributed at about 50 nm, and the pore size increases

with the increase of MCS. The pore size of AAC-4 and AAC-5 is mainly distributed at about 100 nm, and the pore size of HAC-5 is mainly distributed at about 100 nm and 3000 nm. The porosity and pore distribution of AAC and HAC-5 calculated through MIP datas in Fig. 9 are shown in Fig. 10. Porosity of AAC increased from 62.9–63.4%, 63.6%, 63.7% and 63.9%, respectively, with the increase of MCS content from 0–25%, 50%, 75% and 100%. Air voids (above 10000 nm) and mesopores (10–50 nm) content decreased while macropores (50-10000 nm) increased in this case. In summary, the increase of MCS in AAC increased the macropores and porosity of AAC, which is consistent with the test results of physical properties. The increase of porosity will increase the thermal conductivity of AAC and decrease the mechanical properties. After HAC-5 was cured in autoclave (216°C, 2 MPa) for 8 hours to form AAC-5, the porosity increased from 57.9% (HAC-5) to 63.9% (AAC-5), air voids and macropores content decreased while mesopores increased. The results show that in the process of high-pressure curing, the hydrated products fill the large pores of the matrix, which refine the pores of the matrix, and the matrix also forms additional pores due to hydration reaction.

3.4.2. Mineral compositions

XRD patterns of AAC and HAC-5 were shown in Fig. 11. Tobermorite, quartz, katoite, anhydrite and calcite are the main minerals in AAC. MCS has no effect on the mineral phase types of AAC. The amount and crystallinity of tobermorite have a significant impact on all aspects of AAC properties (Matsui et al. 2011; Isu et al. 1995; Mostafa 2005), which is the most important crystallization product of AAC. It can be seen from Fig. 11 (b) that the crystallinity of tobermorite in AAC-5 is high, that is, AAC-5 sample has good physical and mechanical properties and thermal conductivity. The characteristic diffraction peaks of AAC-1 and AAC-5 mineral phases are consistent, as shown in Fig. 11(a). The main mineral phases of hac-5 are quartz, kuzelite, ettringite and portland. Quartz is the mineral phase of fly ash, and kuzelite, ettringite and portland are formed by hydration reaction in the early stage of HAC. At 216 ℃ and 2MPa, after autoclave curing for 8 hours, the characteristic peaks of kuzelite, ettringite and portland mineral phases in HAC-5 disappeared, and the characteristic peaks of tobermorite, katoite, anhydrite and calcite appeared. This is because under high pressure conditions, AFt, C-S-H gel, gypsum and silicate hydration products in HAC-5 react in autoclave reaction, and finally convert to tobermorite, katoite and anhydrite. During the formation of tobermorite, katoite and anhydrite in the system, heat will be released, new pores will be generated in the matrix and the porosity of the matrix will be improved. This is consistent with MIP results.

TG and DTG curves of AAC-5 and HAC-5 are shown in Fig. 12. In HAC-5 the main weight loss is located at about 100°C (C-S-H gels dehydrated), 120°C (AFt dehydrated) and 450°C ($Ca(OH)_2$ dehydroxylated) (Luo et al. 2019; Luo et al. 2020), respectively. As shown in Fig. 12(b), the main weight loss of AAC-5 is at about 50–300 ℃ (the loss of adsorbed water and bound water) (Cai et al. 2021), 100–350°C (tobermorite dehydrated) and 850°C (exothermic transformation of tobermorite into β- wollastonite), 400°C (katoite decomposed) (Jiang et al. 2021), 750°C (calcite decomposed). Under high pressure conditions, AFt, C-S-H gel, gypsum and silicate hydration products in HAC-5 react in autoclave reaction, and finally convert to tobermorite, katoite and anhydrite. The results are consistent with the XRD results.

Figure 13 shows the morphology of HAC-5 (a, c) and AAC-5 (b, d). There were a small amount of dense plate products (A), gelatinous (B), needle-stick (C), bamboo leaf (D), regular hexagonal shape (E), filamentous (F) and irregular block (G) products in the samples. EDS data of the labeled area in Fig. 13 are shown in Table 3. In HAC-5, the gelatinous and filamentous products containing Ca, Si and Al can be identified as C-S-H, the dense plate products can be identified as $Ca(OH)_2$, the needle-stick products can be identified as AFt. HAC-5 was mainly composed of C-S-H gel, AFt and $Ca(OH)_2$. In AAC-5, the bamboo leaf products can be identified as tobermorite, the regular hexagonal shape products can be identified as $CaCO_3$, the irregular block products can be identified as katoite. At 216 ℃ and 2MPa, after autoclave curing for 8 hours, AAC-5 was mainly composed of tobermorite, $CaCO_3$, and katoite. This is because under high pressure conditions, AFt, C-S-H gel, gypsum and silicate hydration products in HAC-5 react in autoclave reaction, and finally convert to tobermorite and katoite. SEM and EDS data were consistent with TG and XRD results.

Table 3
EDS datas of red areas in SEM images

Area	Element, Atomic %					
	O	Mg	Al	Si	Ca	S
A	62.87	0.60	0.48	2.24	33.81	-
B	55.04	0.51	0.31	15.31	28.83	-
C	62.84	0.31	7.50	0.45	26.30	2.60
D	53.79	-	4.05	20.94	21.12	-
E	74.26	0.02	0.01	0.09	25.62	-
F	78.37	-	0.99	4.80	15.84	0.01
G	75.23	0.02	6.05	3.15	14.2	1.35

4. Conclusion

In this study, MCS were used to produce AAC. The CaO activity in MCS was higher than that of lime, and the heat release of MCS was equivalent to that of lime.

MCS can not only improve the fluidity of slurry, but also enhance the gas-foaming rate. When the content of MCS increased from 0 to 100%, the fluidity of slurry increased by 28% and the foaming rate increased by 27%.

Replacing lime with MCS can improve the pore distribution of AAC, reduce the number of mesopores and air voids, increase the number of macropores and improve the porosity of matrix. When the content of MCS increased from 0 to 100%, the macropores of AAC increased by 15.1% and the mesopores and air voids decreased by 9.3% and 5.8%.

Under the same mix proportion, with the increase of MCS content, the density and strength of AAC decrease and the thermal insulation performance increase. When the MCS content is 100%, the AAC density is 594 kg/m^3, the compressive strength is 3.6 MPa and the thermal conductivity is 0.141 $W \cdot m^{-1} \cdot K^{-1}$. The produced AAC meets B06 A3.5 in Chinese standard GB 11968 – 2019. When producing AAC with the same bulk density, using MCS as calcareous material can reduce the content of aluminum powder to a certain extent and save the production cost, which is compared with lime.

Declarations

Acknowledgement

This work was supported by Sichuan Science and Technology Program (No.2019ZDZX0024).

Funding

This work was supported by Sichuan Science and Technology Program (No.2019ZDZX0024).

Author Contributions

Kai Luo: Methodology, Project administration, Writing-Original Draft, Writing- Reviewing and Editing, Ke Peng: Investigation, Software, Jun Li: Data Curation, Investigation, Writing- Reviewing and Editing, Zhongyuan Lu: Conceptualization, Investigation, Jun Jiang: Supervision, Investigation.

Corresponding author

Jun Li. Email: lijun@swust.edu.cn

Ethics approval

All experiments were in accordance with the current Chinese legislation.

Consent to participate

The authors have consent to participate.

Consent for publication

The authors have consent to publish.

Competing interests

The authors declare no competing interests.

References

1. Albayrak, M., A. Yörükoğlu, S. Karahan, S. Atlıhan, H. Yılmaz Aruntaş, and İ. Girgin. 2007. Influence of zeolite additive on properties of autoclaved aerated concrete. Build. Environ. 42(9), 3161-3165.
2. Amnadnua, K., W. Tangchirapat, and C. Jaturapitakkul. 2013. Strength, water permeability, and heat evolution of high strength concrete made from the mixture of calcium carbide residue and fly ash. Mater. Des. 51, 894-901. https://doi.org/10.1016/j.matdes.2013.04.099.
3. Ashish, D.K., and S.K. Verma. 2019. Cementing Efficiency of Flash and Rotary-Calcined Metakaolin in Concrete. Journal of materials in civil engineering 31(12):04019307.1-04019307.12.
4. Ashish, D. K. 2019. Concrete made with waste marble powder and supplementary cementitious material for sustainable development. Journal of Cleaner Production, 211, 716-729.
5. Bhosale, A., N. P. Zade, P. Sarkar, and R. Davis. 2020. Mechanical and physical properties of cellular lightweight concrete block masonry. Construction and Building Materials, 248, 118621.
6. Bhosale, A., N.P. Zade, R. Davis, and P. Sarkar. 2019. Experimental Investigation of Autoclaved Aerated Concrete Masonry. *J. Mater. Civ. Eng.*, 31(7), 04019109.
7. Chindaprasirt, P., A. Kampala, P. Jitsangiam, and S. Horpibulsuk. 2020. Performance and evaluation of calcium carbide residue stabilized lateritic soil for construction materials. Case Studies in Construction Materials 13, e00389. https://doi.org/10.1016/j.cscm.2020.e00389.
8. Cai, L., T. Tang, M. Liu, and D. Xie. 2020. Comparative study of carbide slag autoclaved aerated concrete (AAC) manufactured under thermal oven and microwave precuring process: Foaming course, rough body strength and physic-mechanical properties. Constr. Build. Mater. 236, 117550. https://doi.org/10.1016/j.conbuildmat.2019.117550.
9. Cai, Q., B. Ma, J. Jiang, J. Wang, Z. Shao, Y. Hu, B.Qian, and L. Wang. 2021. Utilization of waste red gypsum in autoclaved aerated concrete preparation. Construction and Building Materials 291, 123376.
10. Cong, P., and L. Mei. 2021. Using silica fume for improvement of fly ash/slag based geopolymer activated with calcium carbide residue and gypsum. Construction and Building Materials 275, 122171.
11. Dulaimi, A., H.K. Shanbara, H. Jafer, and M. Sadique. 2020. An evaluation of the performance of hot mix asphalt containing calcium carbide residue as a filler. Constr. Build. Mater. 261, 119918. https://doi.org/10.1016/j.conbuildmat.2020.119918.
12. Gong, X.Z., J.Q. Zhang, Z. Wang, D. Wang, J.H. Liu, X.D. Jing, G.Y. Qian, and C. Wang. 2020. Development of calcium coke for CaC2 production using calcium carbide slag and coking coal. Int. J. Miner. Metal. 28(1), 76-87. https://doi.org/10.1007/s12613-020-2049-5.
13. Hanjitsuwan, S., T. Phoo-ngernkham, and N. Damrongwiriyanupap. 2017. Comparative study using Portland cement and calcium carbide residue as a promoter in bottom ash geopolymer mortar. Constr. Build. Mater. 133, 128-134. https://doi.org/10.1016/j.conbuildmat.2017.12.034.
14. Horpibulsuk, S., C. Phetchuay, and A. Chinkulkijniwat. 2012. Soil Stabilization by Calcium Carbide Residue and Fly Ash. J. Mater. Civ. Eng. 24(2), 184-193. http://doi.org/10.1061/(ASCE)MT.1943-5533.0000370
15. Horpibulsuk, S., V. Munsrakest, A. Udomchai, A. Chinkulkijniwat, and A. Arulrajah. 2014. Strength of sustainable non-bearing masonry units manufactured from calcium carbide residue and fly ash.

Construction and Building Materials 71, 210-215.

16. Isu, N., H. Ishida, and T. Mitsuda. 1995. Influence of quartz particle size on the chemical and mechanical properties of autoclaved aerated concrete (I) tobermorite formation. Cem. Concr. Res. 25(2), 243–248. https://doi.org/10.1016/0008-8846(95)00003-8.
17. Jiang, J., Q. Cai, B. Ma, Y. Hu, B. Qian, F. Ma, Z. Shao, Z. Xu, and L. Wang. 2021. Effect of ZSM-5 waste dosage on the properties of autoclaved aerated concrete. Construction and Building Materials 278, 122114.
18. Li, W., and Y. Yi. 2020. Use of carbide slag from acetylene industry for activation of ground granulated blast-furnace slag. Construction and Building Materials 238, 117713. https://doi.org/10.1016/j.conbuildmat.2019.117713.
19. Luo, K., J. Li, Z.Y. Lu, J. Jiang, and Y. Niu. 2019. Effect of nano-SiO2 on early hydration of natural hydraulic lime. Construction & Building Materials 216, 119-127. https://doi.org/10.1016/j.conbuildmat.2019.04.269
20. Luo, K., J. Li, Q. Han, Z. Y. Lu, X. Deng, L. Hou, Y.H. Niu, J. Jiang, X. Xu, and P. Cai. 2020. Influence of nano-SiO2 and carbonation on the performance of natural hydraulic lime mortars. Construction and Building Materials 235, 117411. https://doi.org/10.1016/j.conbuildmat.2019.117411
21. Ma, B.-g., L.-x. Cai, X.-g. Li, S.-w. Jian. 2016. Utilization of iron tailings as substitute in autoclaved aerated concrete: physico-mechanical and microstructure of hydration products. Journal of Cleaner Production 127, 162-171.
22. Matsui, K., J. Kikuma, M. Tsunashima, T. Ishikawa, S.-y. Matsuno, A. Ogawa, and M. Sato. 2011. In situ time-resolved X-ray diffraction of tobermorite formation in autoclaved aerated concrete: Influence of silica source reactivity and Al addition. Cem. Concr. Res. 41(5), 510-519.
23. Mostafa, N.Y. 2005. Influence of air-cooled slag on physicochemical properties of autoclaved aerated concrete. Cem. Concr. Res. 35(7), 1349–1357. https://doi.org/10.1016/j.cemconres.2004.10.011
24. Nshimiyimana, P., A. Messan, Z. Zhao, and L. Courard. 2019. Chemico-microstructural changes in earthen building materials containing calcium carbide residue and rice husk ash. Constr. Build. Mater. 216, 622-631. https://doi.org/10.1016/j.conbuildmat.2019.05.037.
25. Narayanan, N., and K. Ramamurthy. 2000. Structure and properties of aerated concrete: a review. Cem. Concr. Compos 22 (5), 321e329.
26. Peng, Y., Y. Liu, B. Zhan, and G. Xu. 2021. Preparation of autoclaved aerated concrete by using graphite tailings as an alternative silica source. Construction and Building Materials 267, 121792.
27. Phoongernkham, T., C. Phiangphimai, D. Intarabut, S. Hanjitsuwan, N. Damrongwiriyanupap, L. Li, and P. Chindaprasirt. 2020. Low cost and sustainable repair material made from alkali-activated high-calcium fly ash with calcium carbide residue. Constr. Build. Mater. 247, 118543. https://doi.org/10.1016/j.conbuildmat.2020.118543.
28. Phummiphan, I., S. Horpibulsuk, and T. Phoo-Ngernkham. 2017. Marginal lateritic soil stabilized with calcium carbide residue and fly ash geopolymers as a sustainable pavement base material. J. Mater. Civil. Eng. 29(04016195), 1-10. http://doi.org/10.1061/(ASCE)MT.1943-5533.0001708

29. Qu, X., and X. Zhao. 2017. Previous and present investigations on the components, microstructure and main properties of autoclaved aerated concrete – A review. Construction and Building Materials 135, 505-516.
30. Rattanashotinunt, C., P. Thairit, W. Tangchirapat, and C. Jaturapitakkul. 2013. Use of calcium carbide residue and bagasse ash mixtures as a new cementitious material in concrete. Materials & Design 46, 106-111.
31. Wang, C.-l., W. Ni, S.-q. Zhang, S. Wang, G.-s. Gai, and W.-k. Wang. 2016. Preparation and properties of autoclaved aerated concrete using coal gangue and iron ore tailings. Construction and Building Materials 104, 109-115.
32. Wu, R., S. Dai, S. Jian, J. Huang, Y. Lv, B. Li, and N. Azizbek. 2020. Utilization of the circulating fluidized bed combustion ash in autoclaved aerated concrete: Effect of superplasticizer. Constr. Build. Mater. 237, 117644. https://doi.org/10.1016/j.conbuildmat.2019.117644
33. Yang, J., S. Liu, L. Ma, S. Zhao, H. Liu, Q. Dai, Y. Yang, C. Xu X., Xin, X. Zhang, and J. Liu. 2021. Mechanism analysis of carbide slag capture of CO2 via a gas-liquid-solid three-phase fluidization system. Journal of Cleaner Production 279, 123712. https://doi.org/10.1016/j.jclepro.2020.123712.

Figures

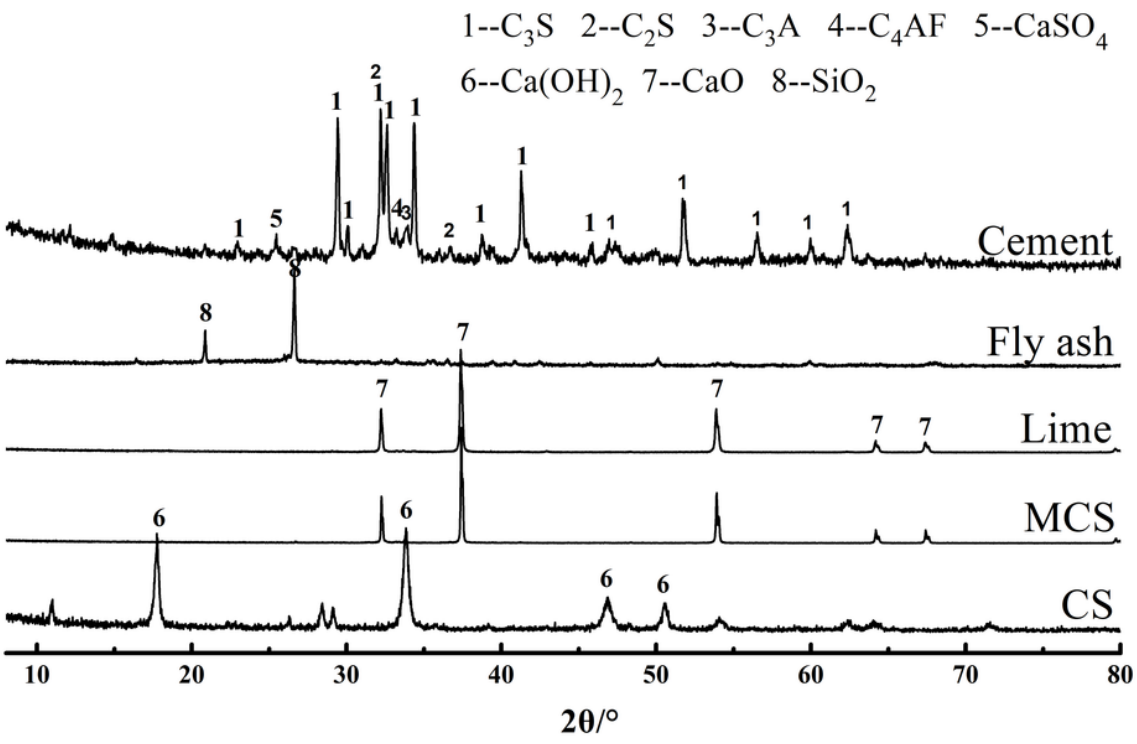

Figure 1

X-ray diffraction pattern of Cement, Fly ash, Lime, MCS and CS

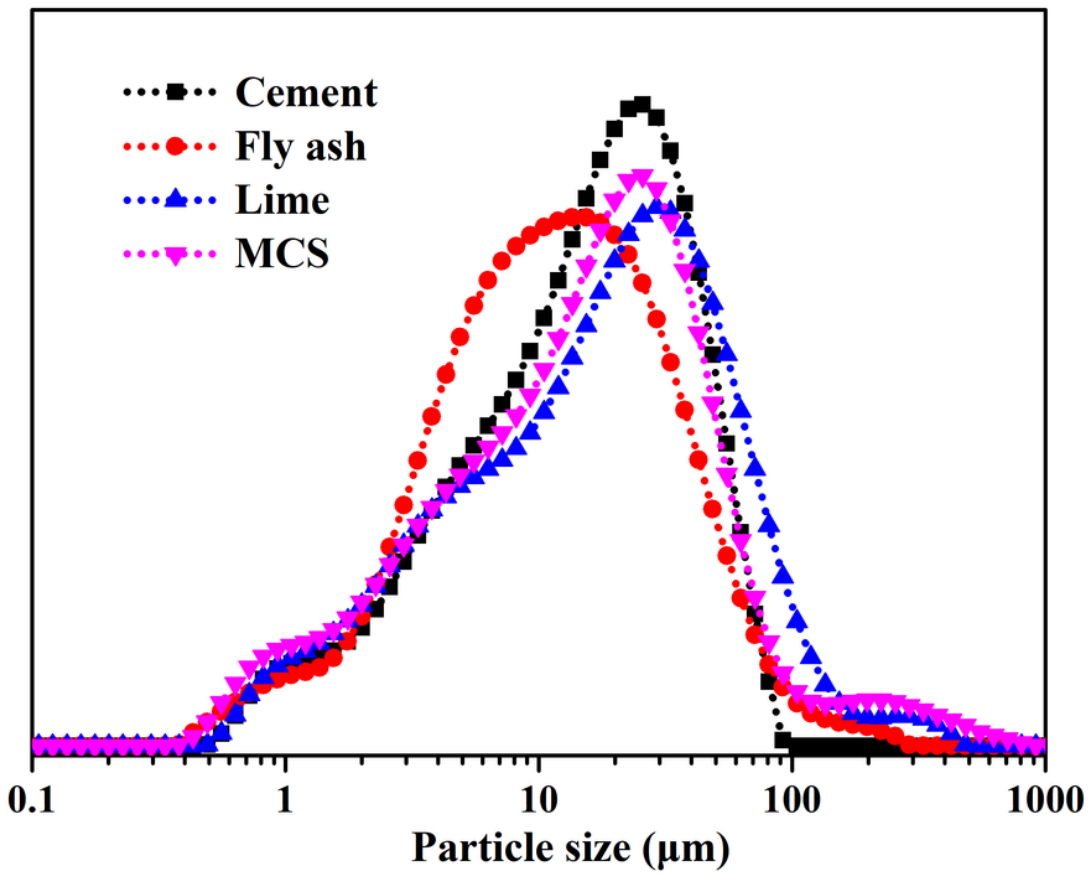

Figure 2

Particle size distributions of cement, fly ash, lime and MCS

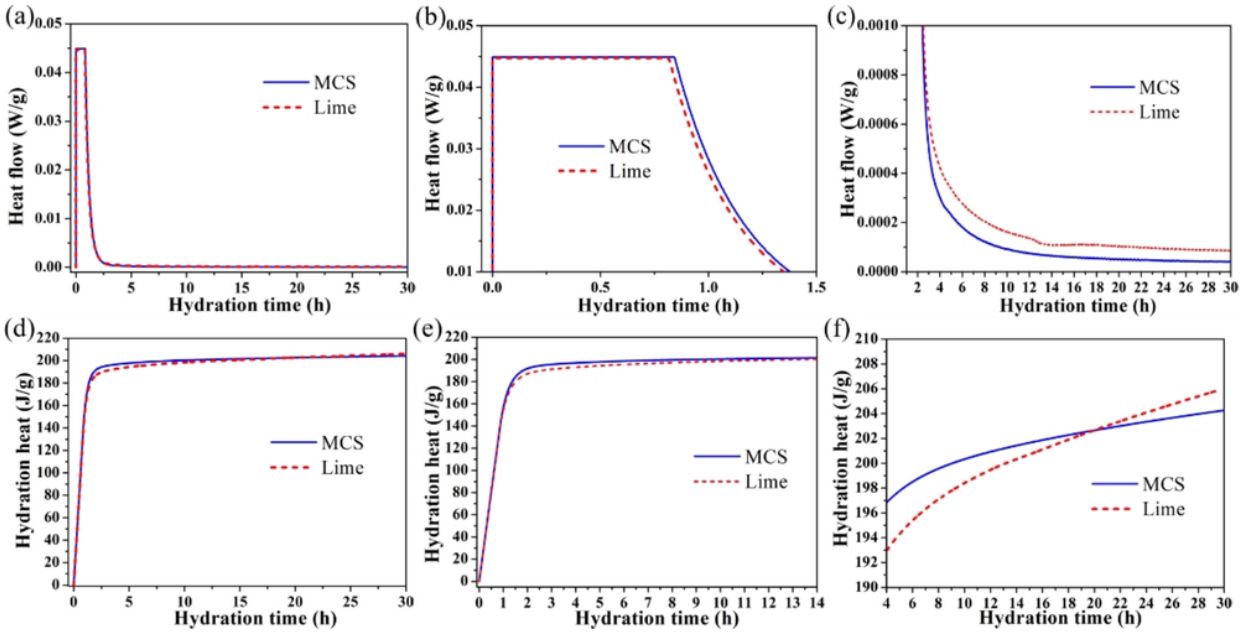

Figure 3

Hydration heat evolution of lime and MCS pastes a 0-30 h, b 0-1.5 h and c 2-30 h, cumulative hydration heat of lime and MCS pastes d 0-30 h, e 0-14 h and f 4-30 h

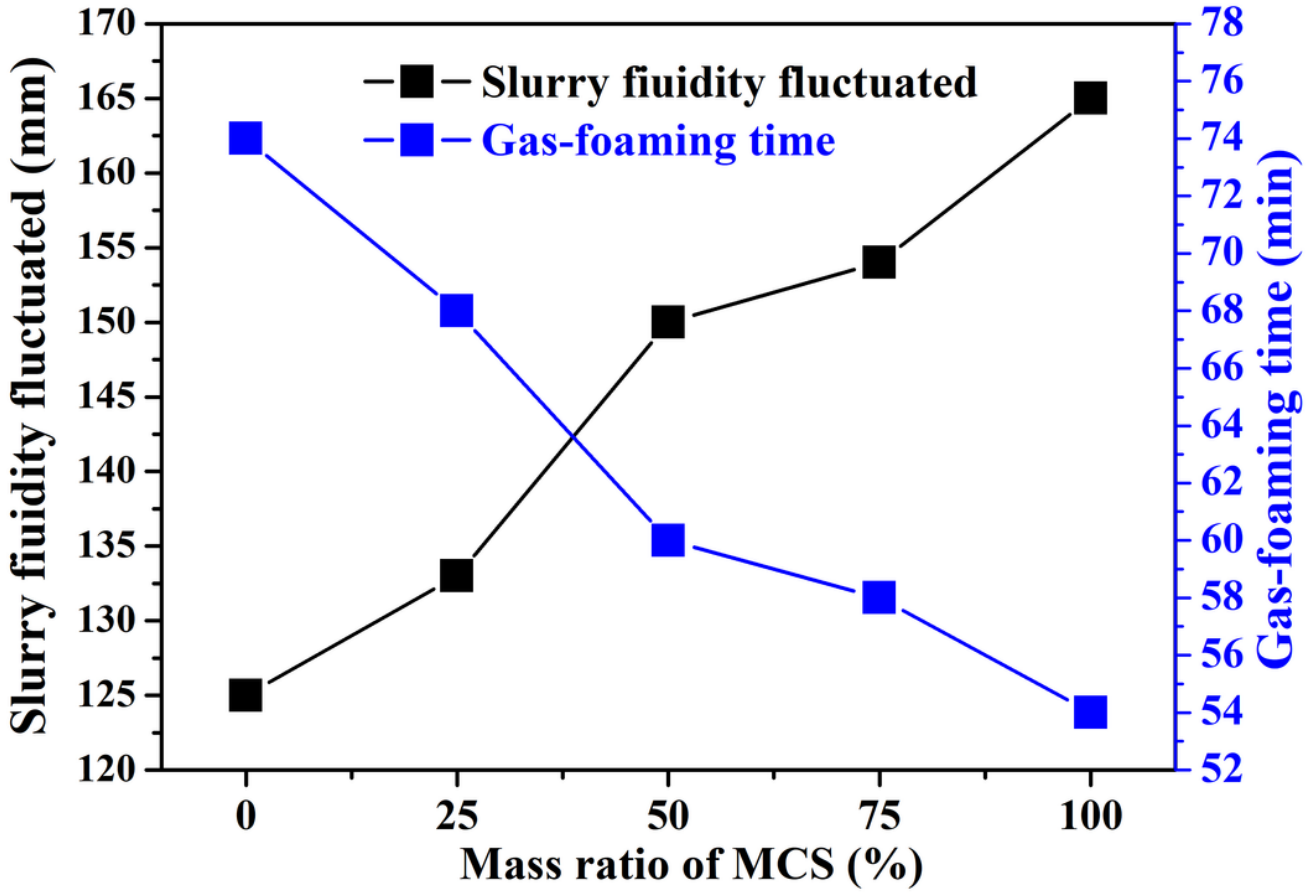

Figure 4

Effects of MCS content on the slurry properties

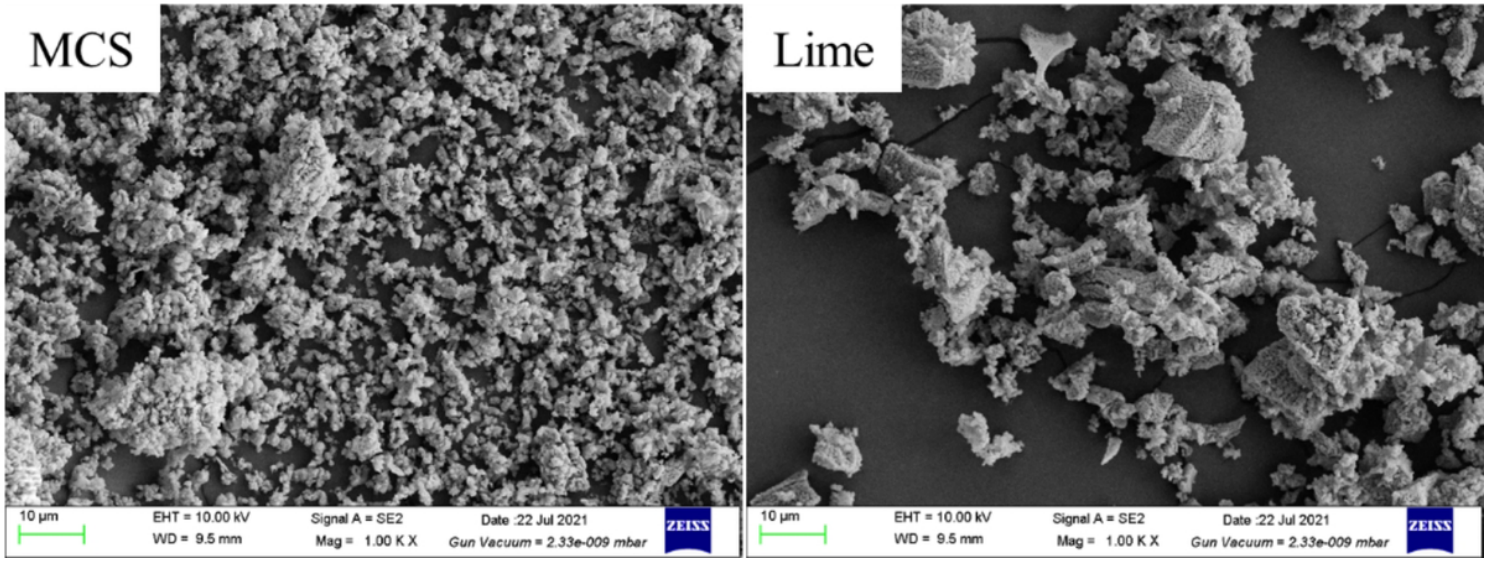

Figure 5

SEM images of MCS and lime

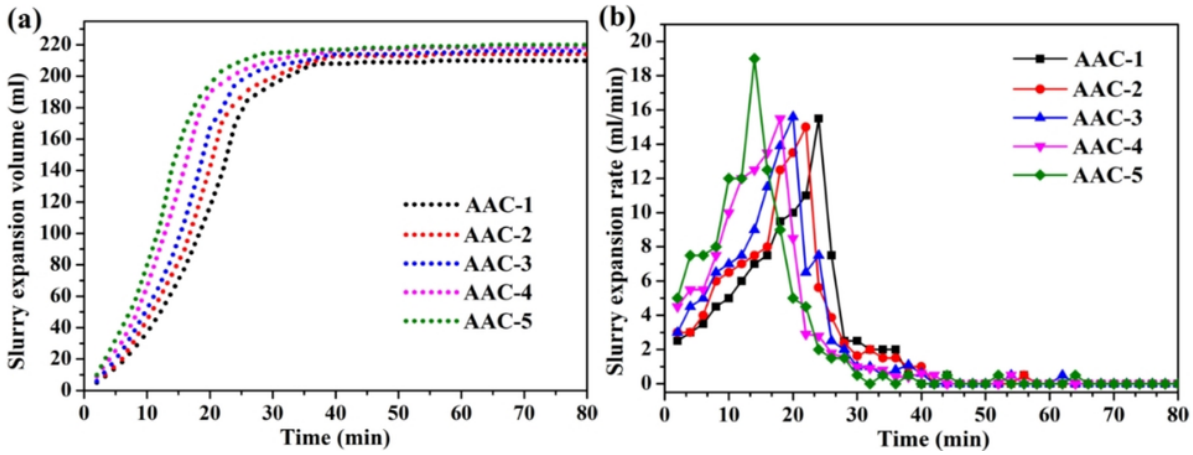

Figure 6

(a) Slurry expansion volume and (b) Expansion rate of different samples

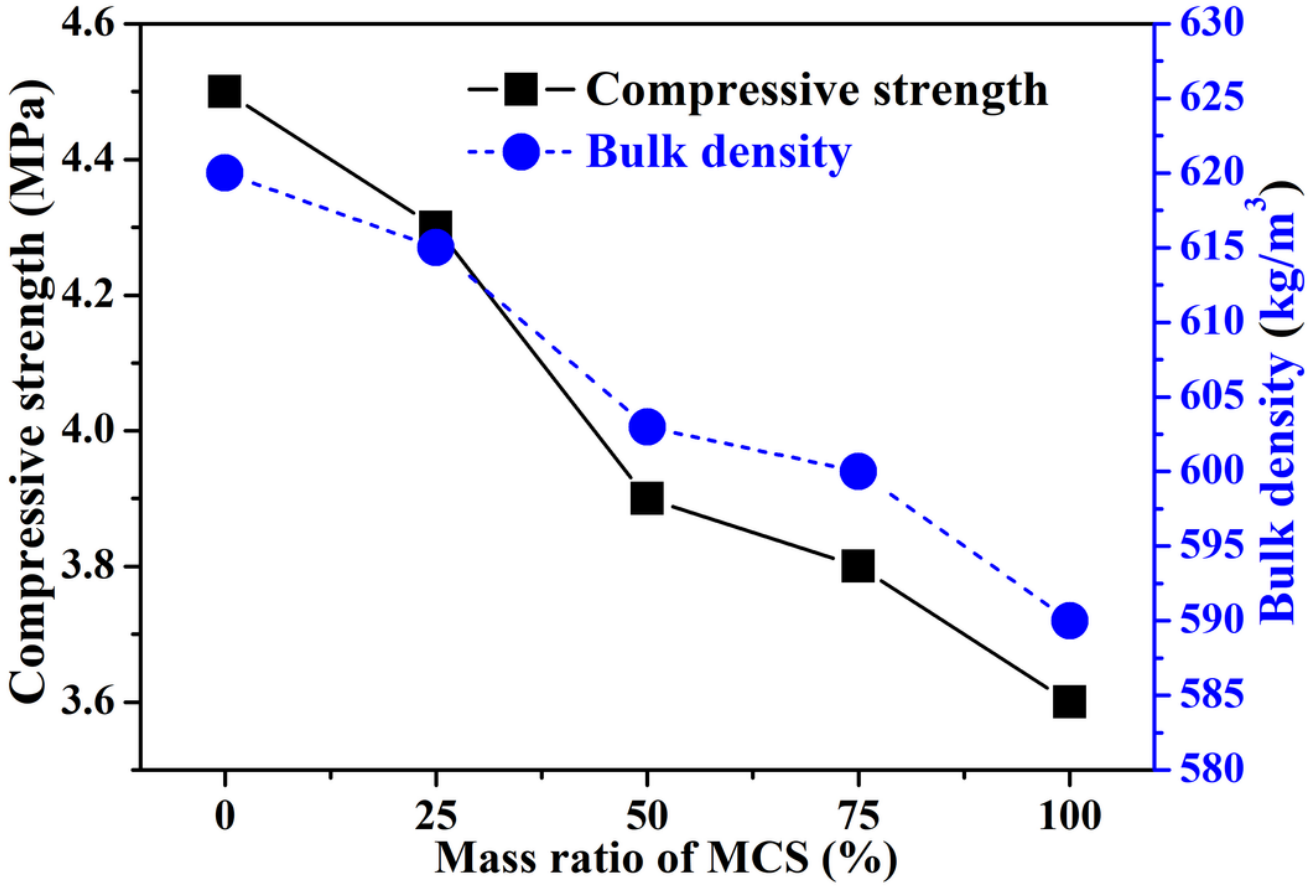

Figure 7

Effects of MCS content on the strength and density of AAC

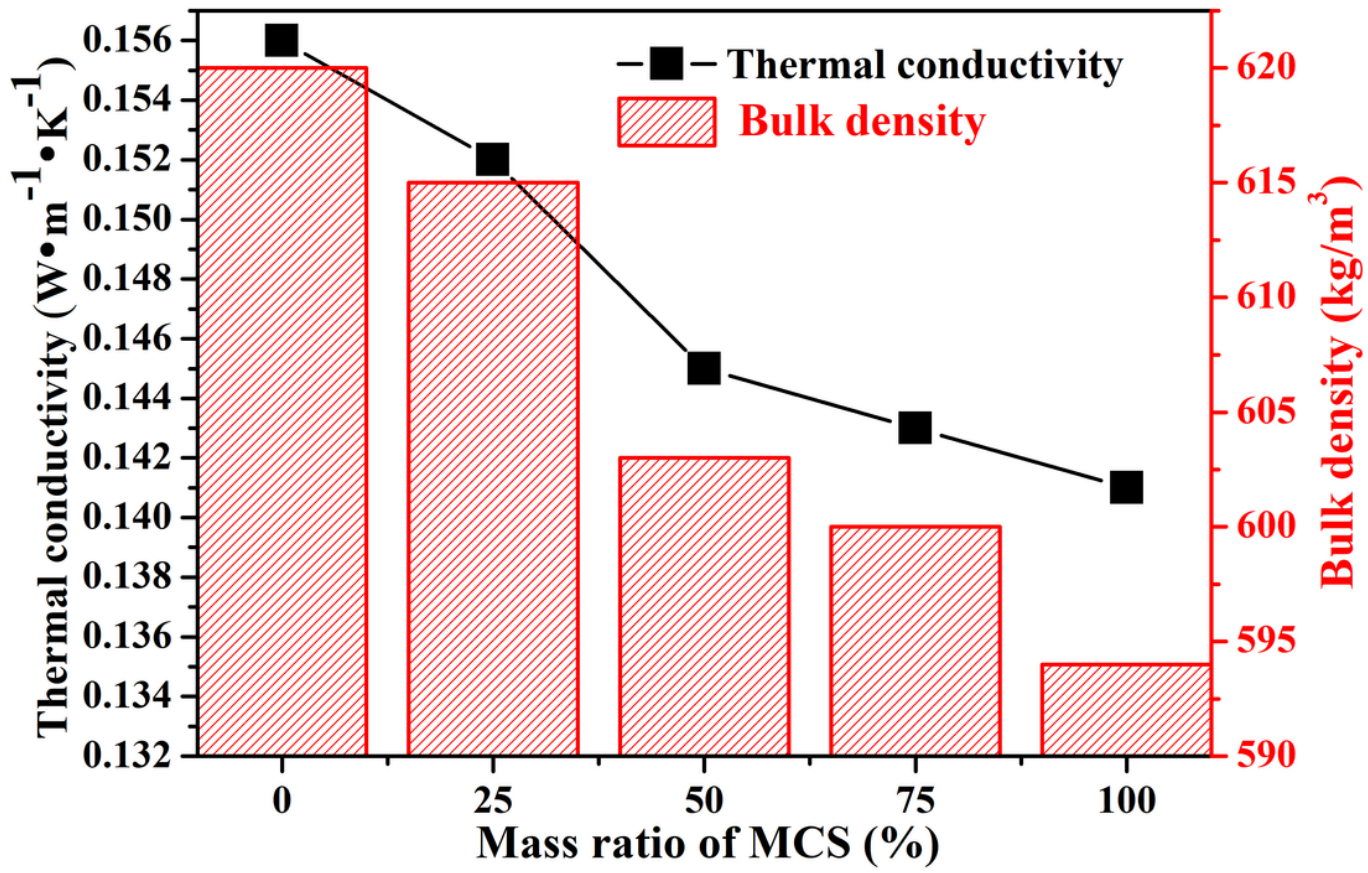

Figure 8

Effects of MCS content on the thermal conductivity and density of AAC

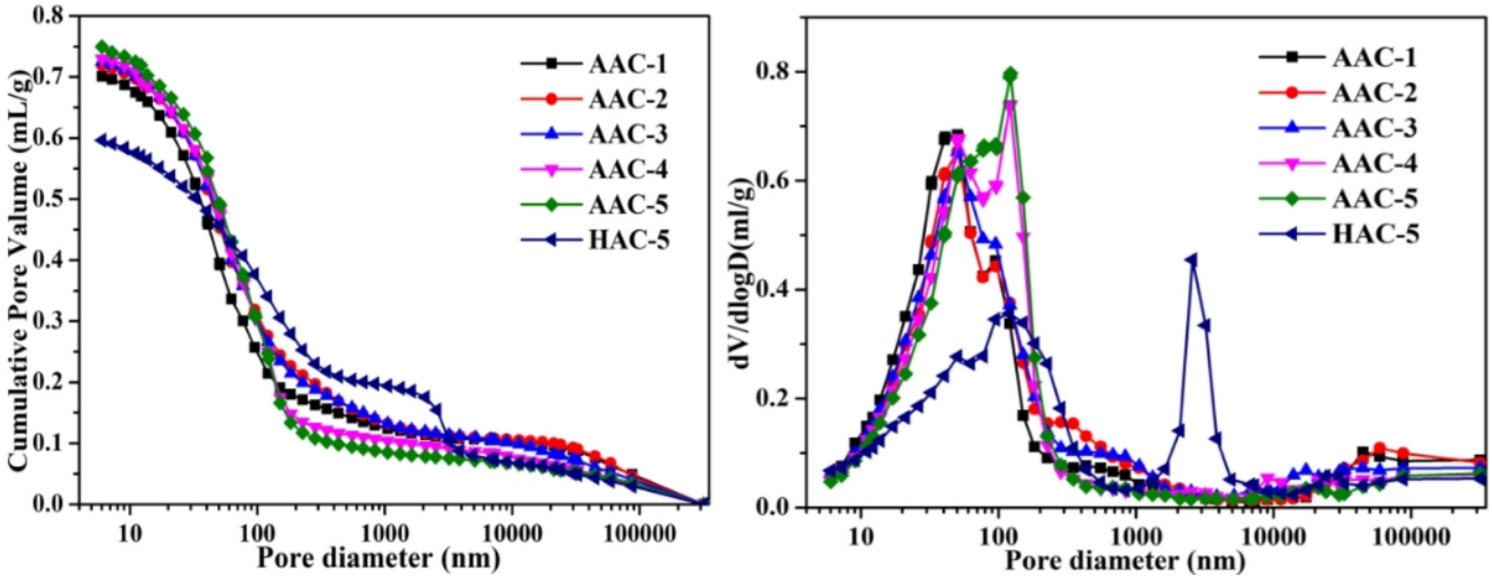

Figure 9

MIP results of AAC and HAC-5

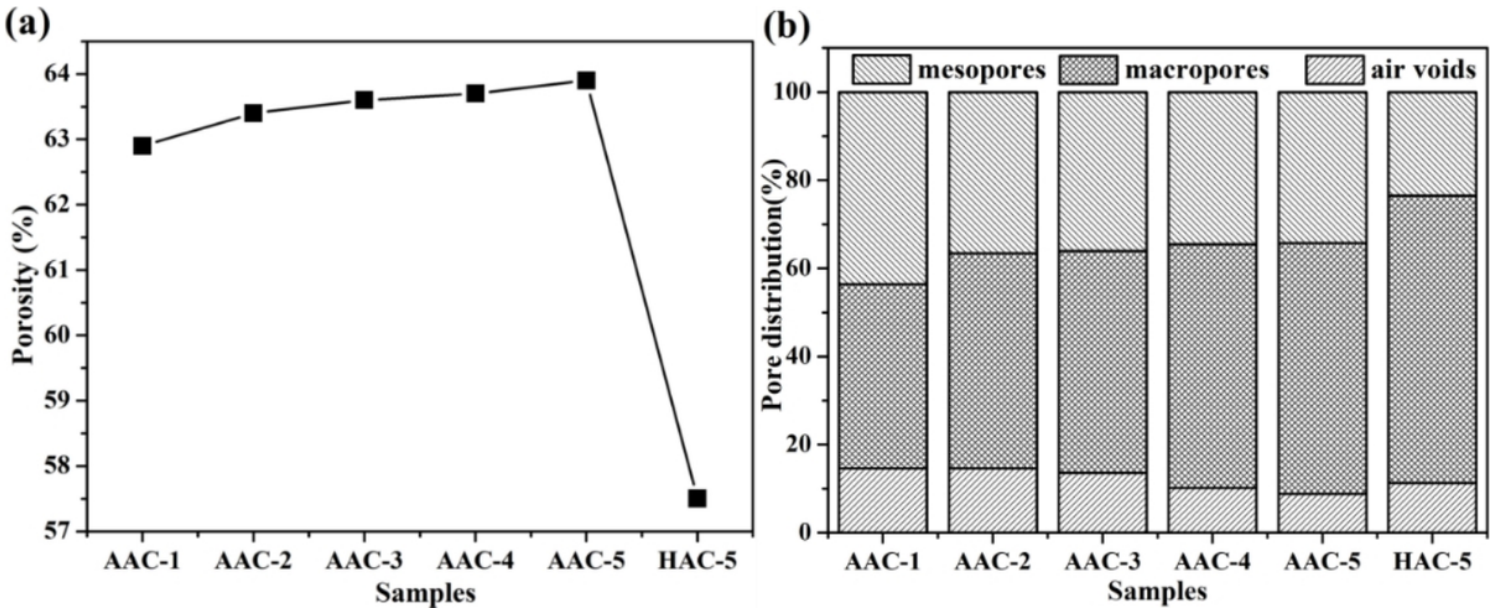

Figure 10

(a) porosity and (b) pore distribution of AAC and HAC-5

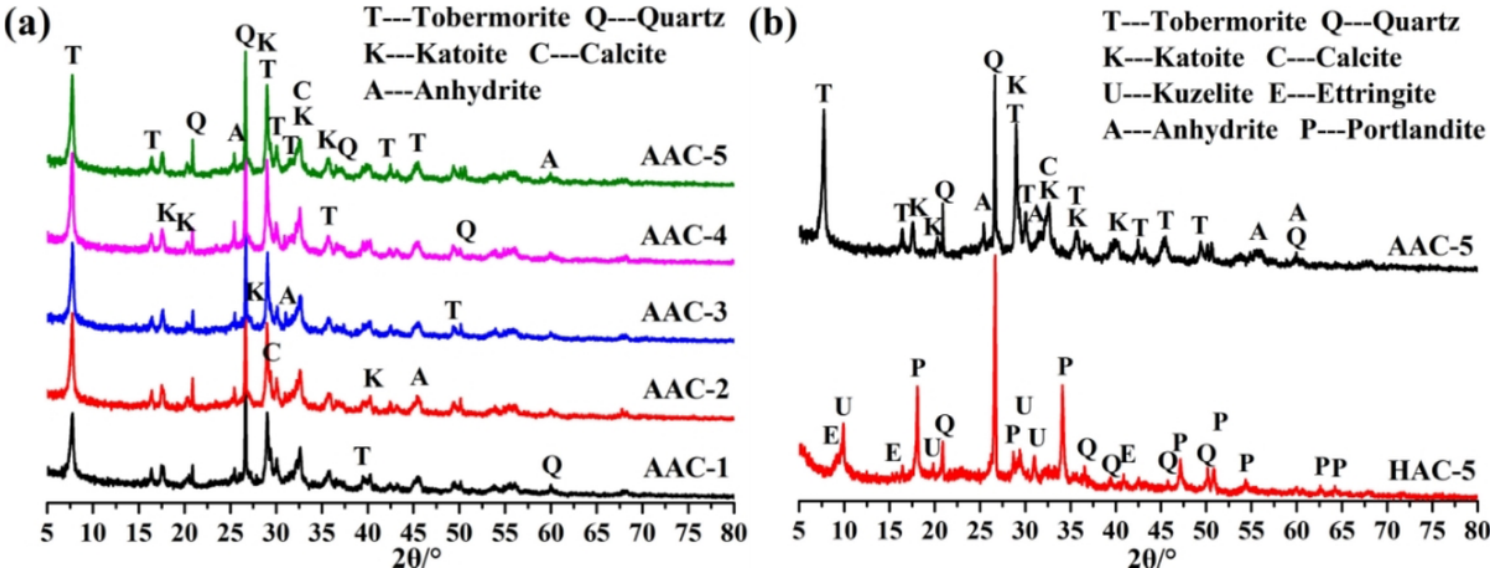

Figure 11

XRD patterns of AAC and HAC-5

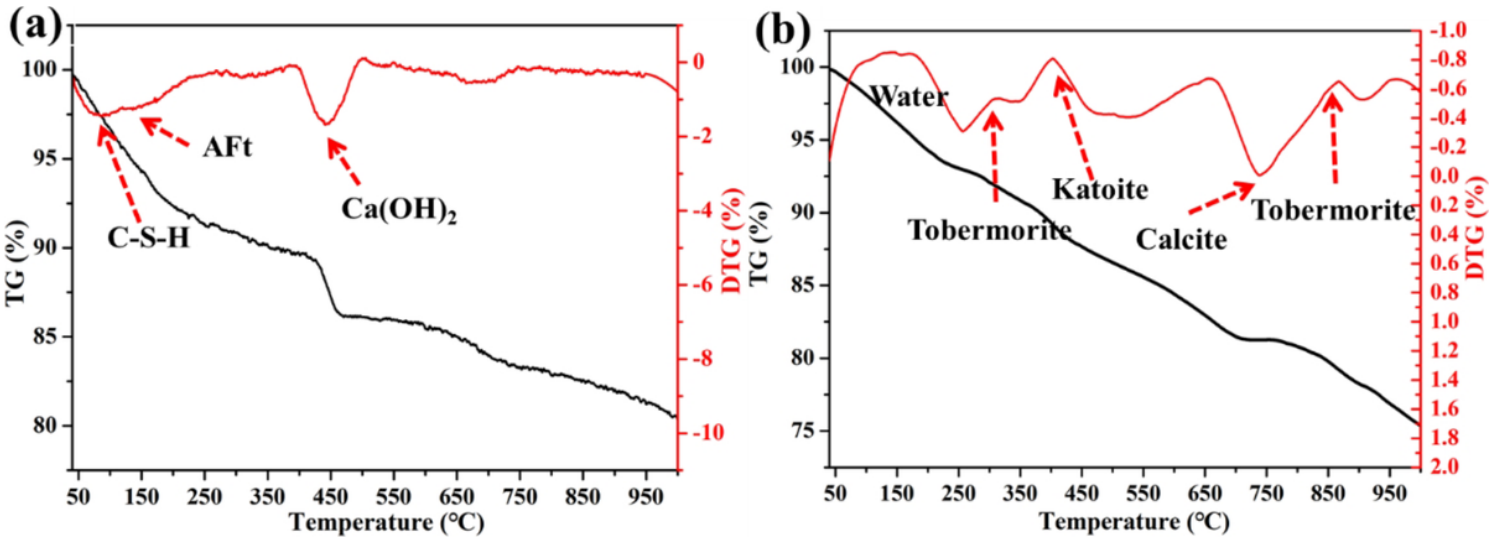

Figure 12

TG/DTG analysis of (a) HAC-5 and (b) AAC sample.

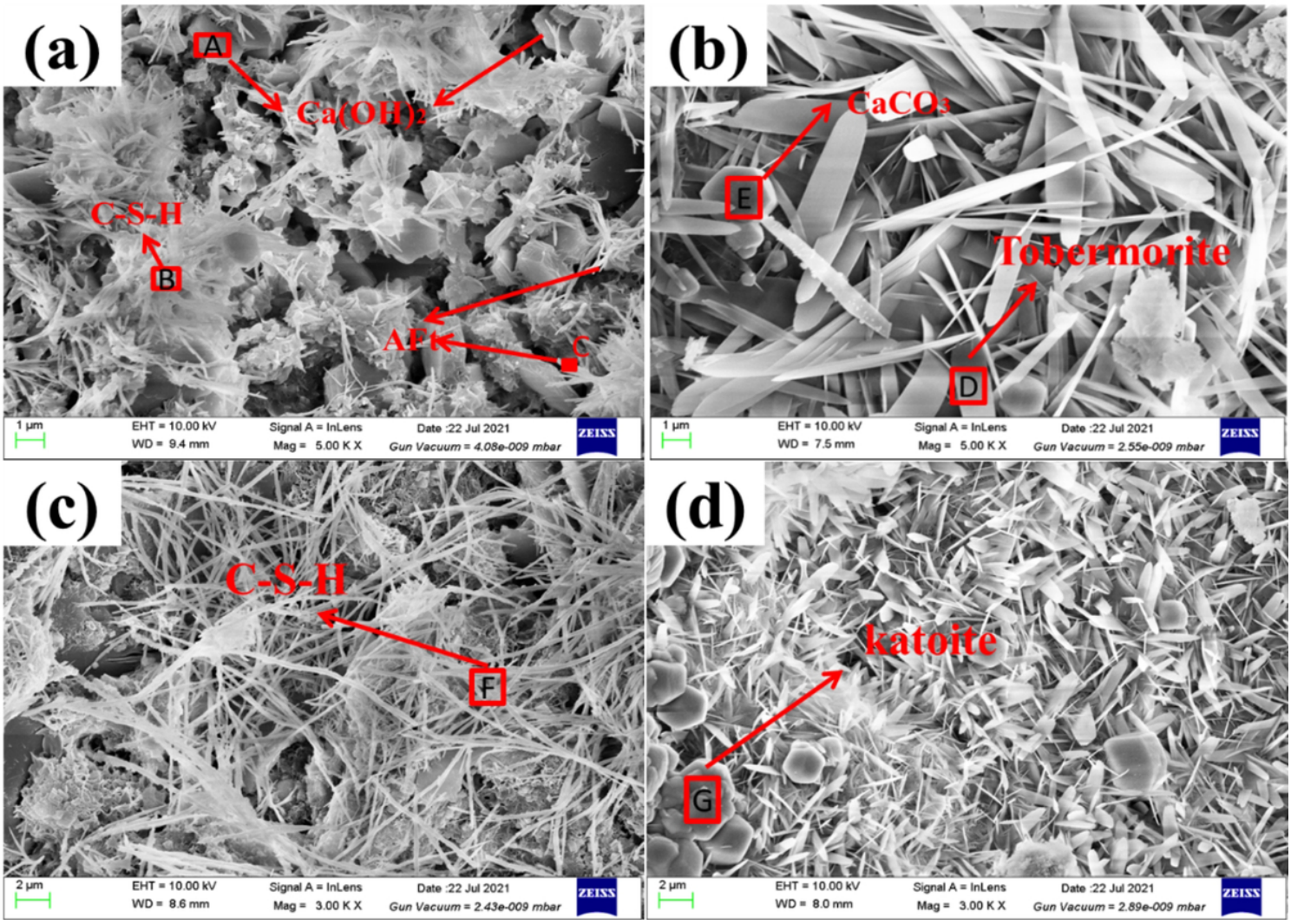

Figure 13

SEM images of HAC-5 (a, c) and AAC-5 (b, d)